

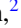


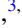





Magnetic anisotropy and spin dynamics in the kagome magnet $\text{Fe}_4\text{Si}_2\text{Sn}_7\text{O}_{16}$: NMR and magnetic susceptibility study on oriented powder

S. Dengre ¹, R. Sarkar ¹, L. Opherden ², T. Herrmannsdörfer ², M. Allison ³, T. Söhnel ^{3,4},
C. D. Ling ⁵, J. S. Gardner ^{6,7} and H.-H. Klauss ^{1,*}

¹*Institute of Solid State and Materials Physics, Technical University of Dresden, 01062 Dresden, Germany*

²*Dresden High Magnetic Field Laboratory (HLD-EMFL), Helmholtz-Zentrum Dresden-Rossendorf, 01328 Dresden, Germany*

³*School of Chemical Sciences, University of Auckland, Auckland 1142, New Zealand*

⁴*The MacDiarmid Institute for Advanced Materials and Nanotechnology, Wellington 6140, New Zealand*

⁵*School of Chemistry, The University of Sydney, Sydney 2006, Australia*

⁶*Songshan Lake Materials Laboratory, Dongguang 523000, China*

⁷*Material Science & Technology Division, Oak Ridge National Laboratory, Oak Ridge, Tennessee 37831, USA*



(Received 2 May 2020; revised 16 November 2020; accepted 24 December 2020; published 19 February 2021)

$\text{Fe}_4\text{Si}_2\text{Sn}_7\text{O}_{16}$ hosts an undistorted kagome lattice of Fe^{2+} ($3d^6$, $S = 2$) ions. We present results of bulk magnetization and Sn nuclear magnetic resonance (NMR) measurements on an oriented $\text{Fe}_4\text{Si}_2\text{Sn}_7\text{O}_{16}$ powder sample oriented in geometries parallel (\parallel) and perpendicular (\perp) to the external applied magnetic field used for orienting the powder (B_{ext}). The bulk susceptibility χ shows a broad peak at $T_N \sim 3$ K associated with antiferromagnetic ordering. NMR spectra indicate the presence of planar anisotropy in the kagome planes. From an analysis of the static NMR shift (K) and dynamic spin-lattice relaxation rate ($1/T_1$) we conclude the presence of dominant magnetic fluctuations in the kagome planes. For the \parallel orientation, K scales linearly with the bulk susceptibility for temperatures down to ~ 4 K, while in the \perp orientation K starts to deviate strongly below $T \sim 30$ K. We associate this deviation with the onset of spin-tilting towards the kagome planes. These correlations are also reflected in the $1/T_1$ data for the \parallel orientation, which starts to decrease below $T \sim 30$ K. In this correlated regime, $T_N < T < \sim 30$ K, we discuss the formation of positive chiral spin correlations in the kagome planes.

DOI: [10.1103/PhysRevB.103.064425](https://doi.org/10.1103/PhysRevB.103.064425)

I. INTRODUCTION

Geometrically frustrated kagome lattice compounds are a subject of intense investigations for both classical and quantum Heisenberg antiferromagnets [1,2]. In the classical case (large-spin multiplicity), a coplanar ground state is selected via an “order by disorder” mechanism [3]. On the basis of second-neighbor J_2 and third-neighbor J_3 interactions, Harris *et al.* predicted that for $J_2 > J_3$ and $J_2 < J_3$ the system selects 120° states of type $\mathbf{q} = 0$ and $\mathbf{q} = \sqrt{3} \times \sqrt{3}$, respectively [4]. In recent years, fractionalized \mathbb{Z}_2 and “jammed” spin-liquid ground states have been proposed [5,6]. In quantum systems ($S = 1/2$), the ground state is discussed in the context of valence bond crystals [7] and gapped or gapless spin liquids [8,9].

$\text{Fe}_4\text{Si}_2\text{Sn}_7\text{O}_{16}$ is an Fe-based synthetic kagome compound with a frustration index $f = |\Theta_{\text{CW}}|/T_N \sim 3.6$. Its structure contains alternately stacked Fe^{2+} ($S = 2$) kagome layers (Fig. 1) and FeSn_6 ($S = 0$) stannate layers [12,13]. The local octahedral environment of the Fe^{2+} ions is similar to the local environments of Dy and Ho in the pyrochlore compounds $\text{Dy}_2\text{Ti}_2\text{O}_7$ and $\text{Ho}_2\text{Ti}_2\text{O}_7$ [10,11]. $\text{Fe}_4\text{Si}_2\text{Sn}_7\text{O}_{16}$ is a classical analog to the well-studied kagome compound herbertsmithite,

$\text{ZnCu}_3(\text{OH})_6\text{Cl}_2$, which is a candidate to realize a quantum spin-liquid state [1,14].

Recent results of neutron scattering and Mössbauer spectroscopy experiments on $\text{Fe}_4\text{Si}_2\text{Sn}_7\text{O}_{16}$ suggest that the Fe moments lie in the kagome planes [15]. Below the ordering temperature $T_N \sim 3$ K, only 2/3 of the spins order antiferromagnetically, while the other 1/3 remain frustrated down to at least 0.1 K [15]. The proposed single- \mathbf{q} propagation vector $(0, \frac{1}{2}, \frac{1}{2})$ breaks the hexagonal symmetry of the lattice. Partially ordered states are also observed in the Heisenberg pyrochlore system $\text{Gd}_2\text{Ti}_2\text{O}_7$ and in the kagome heavy-metal system CePdAl [16,17]. Further, for a kagome spin-ice system with additional J_2 interactions, partially ordered magnetic structures were predicted by Wills *et al.* [18].

The observed partially ordered magnetic structure of $\text{Fe}_4\text{Si}_2\text{Sn}_7\text{O}_{16}$ is in contrast with most predictions for kagome Heisenberg antiferromagnetic (AFM) models [19]. For example, in the Fe kagome jarosite compound $\text{KFe}_3(\text{OH})_6(\text{SO}_4)_2$, Fe^{3+} ($S = 5/2$, $L = 0$) hosts a 120° magnetic structure of type $\mathbf{q} = 0$ with positive chirality (clockwise rotation of spins in a kagome triangle) [20–22]. These moments are canted out of the kagome planes [20–22]. This tilting of Fe^{3+} spins is favorably explained by additional Dzyaloshinskii-Moriya interactions rather than by single-ion anisotropy [4,20,22–28].

To understand the relevant anisotropic interactions in $\text{Fe}_4\text{Si}_2\text{Sn}_7\text{O}_{16}$ we have now performed bulk magnetization and nuclear magnetic resonance (NMR) studies on oriented

*henning.klauss@tu-dresden.de

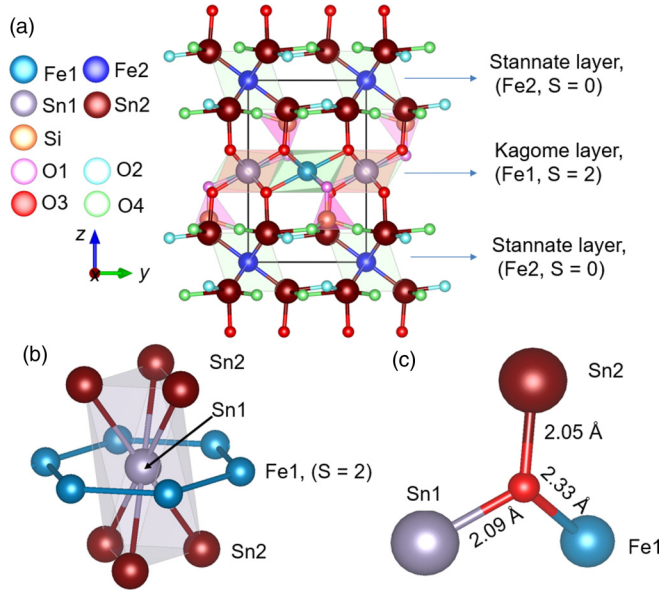


FIG. 1. (a) Crystal structure of $\text{Fe}_4\text{Si}_2\text{Sn}_7\text{O}_{16}$ with the kagome layer made up of FeO_6 (Fe1, O1, O3) and SnO_6 (Sn1, O1, O3) octahedra. Kagome layers are separated by a nonmagnetic layer of FeSn_6 octahedra (Fe2, Sn2). The unit cell is shown by dashed lines. (b) Two Sn sites (Sn1, gray; Sn2, brown) in the crystal. Sn1 is located at the center of the kagome rings formed by Fe1 (blue). Sn2 are located equally above and below the kagome layer. There are six times more Sn2 sites than Sn1 sites. (c) Hyperfine pathways between Fe1 and Sn (Sn1, Sn2) via connecting O3.

and unoriented powder samples. The orientation and fixing of the powdered sample were performed at room temperature. NMR is a powerful microscopic probe that can shed light on the local properties of this system. The NMR shift, K , probes the intrinsic spin susceptibility. The NMR line shape allows us to identify the anisotropic behavior. In addition, the NMR spin-lattice relaxation rate, $1/T_1$, probes the dynamical spin susceptibility, giving crucial information about the low-energy excitations, which in general are enhanced for a frustrated system.

Bulk magnetization shows the presence of dominant AFM interactions. NMR measurements on oriented and unoriented powder samples confirm the presence of planar magnetic anisotropy. Our combined NMR studies on oriented and unoriented powder samples yield insights similar to those that could be obtained from a single crystal, which are not available currently. Our investigations reveal the anisotropic static and dynamic properties of $\text{Fe}_4\text{Si}_2\text{Sn}_7\text{O}_{16}$. The K vs bulk susceptibility plot is linear down to 4 K, confirming the absence of foreign phases. NMR $1/T_1$ shows a weak maximum at ~ 2.5 K due to the critical slowing-down of AFM spin fluctuations.

II. EXPERIMENTAL PROCEDURE

Details of the synthesis of polycrystalline samples of $\text{Fe}_4\text{Si}_2\text{Sn}_7\text{O}_{16}$ were reported previously [13,15]. To prepare an oriented powder sample, approximately similar amounts by volume of $\text{Fe}_4\text{Si}_2\text{Sn}_7\text{O}_{16}$ and Stycast 1266 were thoroughly mixed in a quartz tube of height 2 cm and diameter

0.5 cm. Then the mixture was placed in a homogeneous field of $B_{\text{ext}} = 7$ T for approximately 24 h at room temperature. For comparison, we prepared an unoriented powder sample of similar mass in a similar way. The temperature-dependent zero-field-cooled (ZFC) susceptibility was measured in a Quantum Design superconducting quantum interference device (SQUID) magnetometer. We performed χ measurements of $\text{Fe}_4\text{Si}_2\text{Sn}_7\text{O}_{16}$ over the temperature range from 1.8 to 300 K and up to $B_{\text{ext}} = 5$ T.

NMR experiments were performed using a Tecmag spectrometer at frequencies $f = 42$, 54, and 84 MHz over wide magnetic field and temperature ranges. NMR line shapes of isotopes ^{119}Sn ($I = 1/2$, $\frac{\gamma_N}{2\pi} = 15.868$ MHz/T, 8.58% abundance) and ^{117}Sn ($I = 1/2$, $\frac{\gamma_N}{2\pi} = 15.167$ MHz/T, 7.61% abundance) were measured on oriented and unoriented powder samples using a 90° - τ - 180° pulse sequence. For spin-lattice relaxation rate, $1/T_1$, measurements, we used the saturation recovery method 90° - τ_1 - 90° - τ - 180° pulse sequence. $1/T_1$ experiments were performed at the maxima of the central lines. For the oriented sample, we performed magnetization and NMR experiments by applying $B_{\text{ext}} \parallel B_{\text{ori}}$ and $B_{\text{ext}} \perp B_{\text{ori}}$. These two sets of orientations are hereafter referred to as parallel ($\chi_{\parallel}, B_{\parallel}$) and perpendicular (χ_{\perp}, B_{\perp}), respectively.

III. RESULTS AND ANALYSES

A. Bulk magnetization

An anisotropic magnetic spin system can have a global easy axis (Ising) as in CePd_2As_2 or it can have multiple local easy axes as in kagome spin ice, with easy axes aligned along the line joining the centers of neighboring kagome triangles [18,29]. In an easy-planar (XY) anisotropic system, we expect the spins to align in a particular plane as in the case of $\text{Er}_2\text{B}_2\text{O}_7$ ($B = \text{Ge}, \text{Yb}$) pyrochlores [30,31]. In general, these anisotropic properties can be verified using a single crystal but in the case of unavailability of a single crystal, these anisotropic properties can be studied by performing the powder orientation such that the sample behaves like a pseudo-single crystal.

In the hexagonal $\text{Fe}_4\text{Si}_2\text{Sn}_7\text{O}_{16}$ system, we expect a global planar anisotropy to be present in the kagome plane (xy plane) [15]. In this case, individual grains of polycrystalline sample will show preferential alignment such that xy planes are parallel to B_{ori} [see Fig. 2(a)]. We can write

$$\chi_{\parallel}^m = (1 - \alpha)\chi_{\text{unoriented}} + \alpha(\chi_{xy}^i) \quad (1)$$

and

$$\chi_{\perp}^m = (1 - \alpha)\chi_{\text{unoriented}} + \frac{\alpha}{2}(\chi_{xy}^i + \chi_z^i), \quad (2)$$

where $\chi_{\parallel,\perp}^m$ and $\chi_{z,xy}^i$ are the measured and intrinsic single-crystal susceptibilities, respectively. α is the fraction of the polycrystalline sample which is preferentially oriented along B_{ori} [32].

Contrary to this, in the case of a global easy axis, we expect the z axis of individual grains of the polycrystalline sample to be preferentially aligned along the B_{ori} direction [see Fig. 2(b)] [32–34], and we can write

$$\chi_{\parallel}^m = (1 - \alpha)\chi_{\text{unoriented}} + \alpha(\chi_z^i) \quad (3)$$

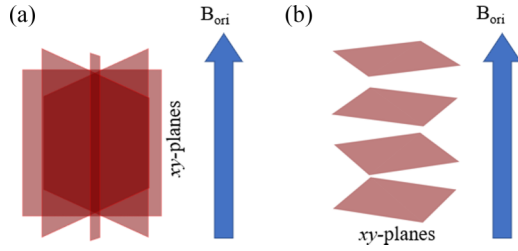


FIG. 2. Schematic of the expected orientation of a polycrystalline sample with respect to the applied field B_{ori} . For an ideal case and a hexagonal system, the alignment of xy planes in the case of (a) global easy-plane and (b) global easy-axis anisotropy, respectively.

and

$$\chi_{\perp}^m = (1 - \alpha)\chi_{\text{unoriented}} + \alpha(\chi_{xy}^i). \quad (4)$$

Since B_{ori} is the driving force for crystal orientation, in both cases we have $\chi_{\parallel}^m > \chi_{\perp}^m$. Independent of the value of α , from Eqs. (1)–(4), for the global easy-axis and global easy-plane cases, we obtain the following relationships:

$$\chi_{\text{unoriented}}^m = \frac{2}{3}\chi_{xy}^i + \frac{1}{3}\chi_z^i = \frac{1}{3}\chi_{\parallel}^m + \frac{2}{3}\chi_{\perp}^m. \quad (5)$$

This shows that from bulk DC susceptibility measurements on oriented samples one cannot distinguish between global easy-axis and global easy-plane anisotropy.

Figure 3 shows that the measured and calculated χ at $B_{\text{ext}} = 100$ mT measured on oriented and unoriented powder samples are consistent. All curves exhibit a broad maximum at ~ 3 K reflecting the AFM transition. The anisotropic behavior of $\text{Fe}_4\text{Si}_2\text{Sn}_7\text{O}_{16}$ persists for B_{ext} up to 5 T (see Supplemental Material [35]). It is lower compared to the planar kagome compound vesigneite, where the spin lies in the plane [36,37].

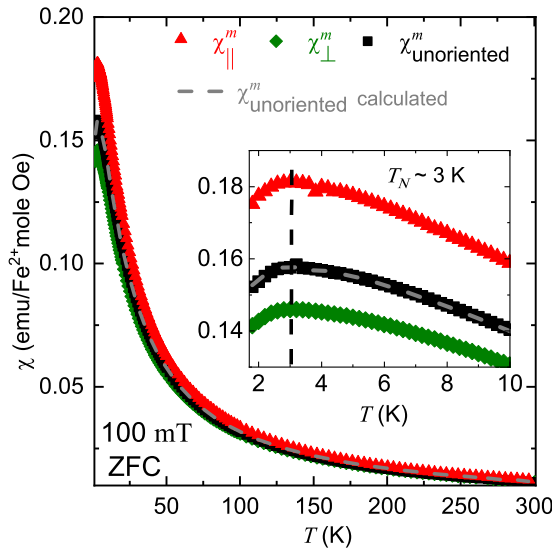


FIG. 3. ZFC magnetic susceptibilities (χ) for unoriented (black) and oriented (red, olive green) samples vs temperature measured in a field of 100 mT. Inset: Low-temperature data. The dashed black line represents the broad AFM transition at $T_N \sim 3$ K. The dashed gray line represents the estimated $\chi_{\text{unoriented}}^m$ per Eq. (5).

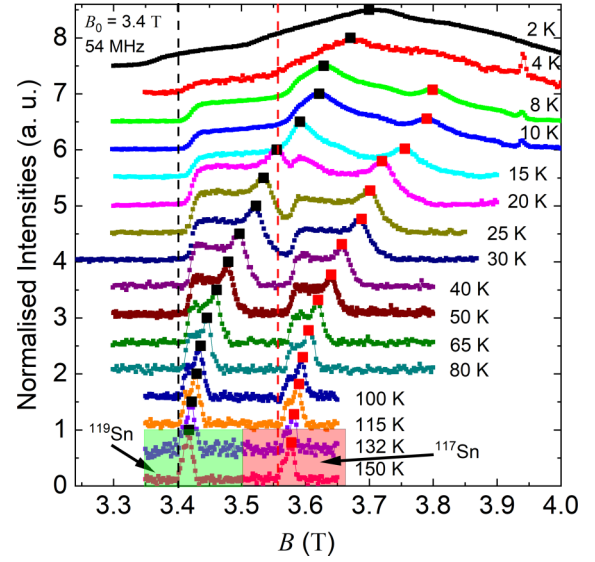


FIG. 4. Temperature dependence of $^{119/117}\text{Sn}$ spectra measured at 54 MHz in an unoriented powder sample. At 150 K, the green- and red-shaded regions show similar signals coming from two isotopes of ^{119}Sn and ^{117}Sn , respectively. The dashed black and red lines represent the peak positions for the diamagnetic ^{119}Sn and ^{117}Sn isotopes, respectively. Filled squares show the peak positions on the right side of the individual $^{119/117}\text{Sn}$ spectra.

For all measured fields, the calculated Θ_{CW} values from the Curie-Weiss law analysis of χ^{-1} are negative, indicating the presence of dominating AFM interactions [35]. Further, for higher external fields, $B_{\text{ext}} \geq 1$ T, in the \parallel (\perp) orientation the calculated values $\mu_{\text{eff, Fe}^{2+}} \sim 5.25\mu_B$ ($5.15\mu_B$) $> \mu_{\text{spin}} = 4.9\mu_B$, and thus we conclude that the orbital moment is not fully quenched.

B. $^{119/117}\text{Sn}$ NMR spectra

We performed $^{119/117}\text{Sn}$ NMR studies on $\text{Fe}_4\text{Si}_2\text{Sn}_7\text{O}_{16}$ for $f = 42, 54,$ and 84 MHz on oriented and unoriented powder samples. Figure 4 shows the temperature dependence of $^{119/117}\text{Sn}$ spectra of an unoriented powder sample measured at $f = 54$ MHz. At 150 K, we observed similar signals from ^{119}Sn and ^{117}Sn isotopes (see Fig. 4). These signals are separated due to the difference in their γ_N values as $f = \gamma_N B_0$ with reference field B_0 . Both isotopes give similar experimental information. Since the natural abundance of ^{119}Sn is higher than that of ^{117}Sn , without loss of any information we focused our analysis on the ^{119}Sn signal. Hereafter we refer to measurements at $f = 42, 54,$ and 84 MHz using $B_0 = 2.64, 3.4,$ and 5.28 T, respectively. The B_0 values are calculated with respect to the diamagnetic reference of ^{119}Sn .

The broadening in the unoriented sample is due to the randomly oriented polycrystalline sample. Since $\text{Fe}_4\text{Si}_2\text{Sn}_7\text{O}_{16}$ has a hexagonal symmetry ($a = b$) the probability of the external field B_{ext} being parallel to the kagome planes is twice the probability of its being perpendicular to the kagome planes. Hence the right-hand part with a higher intensity and the left-hand part with a lower intensity of the unoriented sample

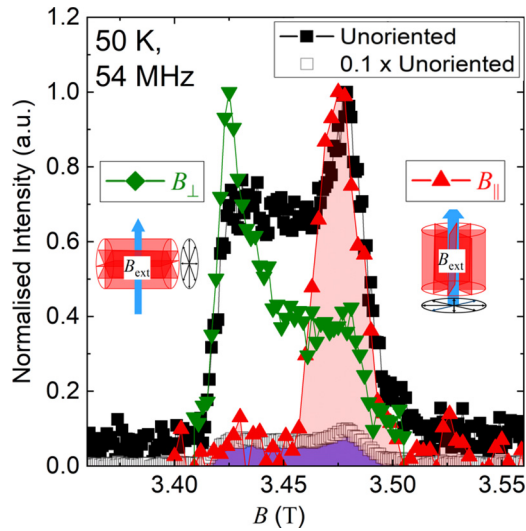


FIG. 5. ^{119}Sn spectrum measured at $B_0 = 3.4$ T (54 MHz) for unoriented (filled black squares) and oriented (\parallel , filled red triangles; \perp , filled olive-green diamonds) samples. Open black squares show the one-tenth intensities from the unoriented sample and confirm a high degree of orientation, $\sim 79\%$, of the oriented powdered sample (see the text). Red planes on the left and right show the expected geometry of kagome planes with respect to B_{ext} for the B_{\perp} and B_{\parallel} orientations, respectively.

spectrum represent the ^{119}Sn signal for $B_{\text{ext}} \parallel$ kagome planes and $B_{\text{ext}} \perp$ kagome planes, respectively. This shows that using NMR we can selectively study the static and dynamic properties \parallel and \perp of the kagome planes, even without using a single crystal.

As we move from higher to lower temperatures, we observe a much higher shift in the right-hand peak compared to the left-hand shoulder. Moreover, the spectrum starts to broaden significantly below 30 K and the effect is even stronger below $T_N \sim 3$ K. This suggests that the onset of magnetic correlations starts to develop at 30 K, well above the ordering temperature $T_N \sim 3$ K. Below 20 K, the right-hand part of the ^{119}Sn signal starts to overlap with the left-hand part of the ^{117}Sn signal, which precludes the identification of the peak corresponding to the ^{119}Sn isotope signal. To solve this problem, we performed NMR experiments on the oriented sample.

To estimate the degree of orientation, we compared the NMR spectra of oriented and unoriented powder samples. Figure 5 presents the field-swept ^{119}Sn NMR spectra measured at $B_0 = 3.4$ T (54 MHz) and 50 K for unoriented and oriented (\parallel , \perp) samples, respectively. We see that for the B_{\parallel} orientation, the low-field shoulder intensity is suppressed and the major contribution is from crystallites with $B_{\text{ext}} \parallel$ kagome planes. This confirms that $\text{Fe}_4\text{Si}_2\text{Sn}_7\text{O}_{16}$ has a planar magnetic anisotropy. Further, for the B_{\perp} orientation, we observe that the contribution from $B_{\text{ext}} \perp$ kagome planes is enhanced but the intensities belonging to $B_{\text{ext}} \parallel$ kagome planes are not fully suppressed (see Fig. 5). This is expected, because due to planar anisotropy all polycrystalline samples are aligned such that the kagome planes are along B_{ori} , but these kagome planes are not parallel to each other (see Fig. 5). Therefore, for

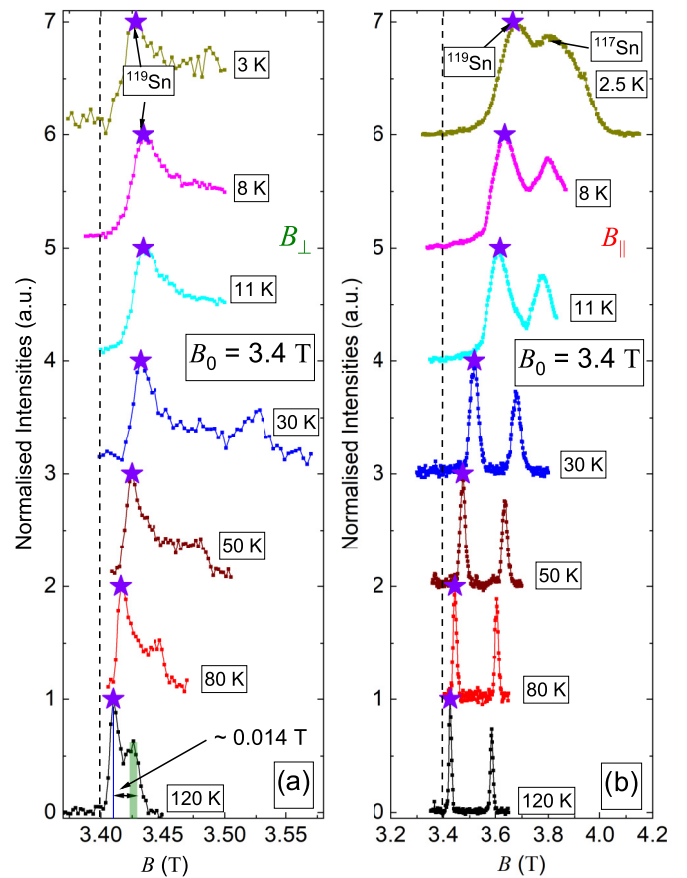


FIG. 6. Temperature variation of the measured spectrum at $B_0 = 3.4$ T (54 MHz) for (a) the \perp and (b) the \parallel orientations. Note that the x -axis scales are different for both orientations. For B_{\parallel} we see well-separated intensities belonging to ^{119}Sn and ^{117}Sn , while for the \perp orientation we focus on the ^{119}Sn signal. For both orientations, purple stars indicate the positions of the peak maxima of the ^{119}Sn signal. In the spectrum at 120 K, for B_{\perp} , the vertical green shading and sharp blue line represent the expected line positions and broadening for the \parallel and \perp orientations, respectively. These line shapes are estimated from dipole-dipole interactions as discussed in the text.

the B_{\perp} orientation, we see some contribution from the planes with $B_{\text{ext}} \parallel$ kagome planes.

In the NMR spectra of the B_{\parallel} orientation (see Fig. 5; filled red triangles), the intensity contribution in the left-hand part of the spectrum (3.4 to 3.45 T) belongs to sample grains with $B_{\text{ext}} \perp$ kagome planes. By dividing the total area under the scaled unoriented powder spectrum (blue-shaded area in Fig. 5) by the total area of the spectrum with the B_{\parallel} orientation (red-shaded area) in the field range of 3.4 to 3.55 T, we find $\alpha \sim 0.79$. This shows that in our sample a high degree of orientation is achieved, such that $\sim 79\%$ of the kagome planes are aligned along B_{ori} .

Figures 6(a) and 6(b) show the temperature variation of the NMR spectra measured at $f = 54$ MHz for the B_{\perp} and B_{\parallel} orientations, respectively. Sn has three NMR active isotopes: ^{119}Sn , ^{117}Sn , and ^{115}Sn . All these isotopes have $S = \frac{1}{2}$ and NMR shows only a central line corresponding to the Zeeman transition ($\frac{1}{2} \leftrightarrow -\frac{1}{2}$). The natural abundance of ^{115}Sn

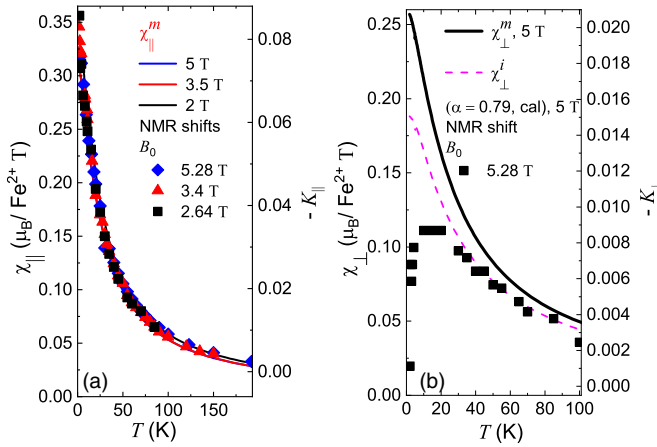


FIG. 7. Temperature dependence of the measured χ and corresponding K for (a) the \parallel and (b) the \perp orientations. The dashed pink line in the right-hand panel shows the estimated χ_{\perp}^i for $\alpha = 0.79$ as discussed in the text.

is 0.35%, and thus the only observed NMR signal is from $^{119/117}\text{Sn}$.

From the structural point of view, there are two nonequivalent Sn sites in $\text{Fe}_4\text{Si}_2\text{Sn}_7\text{O}_{16}$ [Fig. 1(a)]. There are six times more Sn2 than Sn1 sites, therefore the major part of our signal is from Sn2 [Fig. 1(b)]. In addition, the hyperfine interaction pathways for both Sn1 and Sn2 to Fe1 ($S = 2$) are very similar [Fig. 1(c)]; this implies that the Sn1 and Sn2 NMR signals effectively appear as one single peak. We observe that in the oriented sample, NMR signals from ^{119}Sn and ^{117}Sn isotopes are well separated for B_{\parallel} , even for $T < 20$ K. This allows us to accurately measure the position of maxima for both B_{\parallel} and B_{\perp} orientations.

C. NMR shift (K)

From the positions of the maxima we calculated the temperature dependence of the ^{119}Sn NMR shift. The NMR shift K is defined for frequency sweep measurements as $K = (f - f_0)/f_0$, where f is the temperature-dependent resonance frequency and f_0 is the temperature-independent diamagnetic reference. Typically, in the case of field sweep measurements, we estimate $-K = (B - B_0)/B_0$ from the observation of the NMR peak at field B , with $B_0 = f_0/\gamma_N$ being the reference diamagnetic field. For both orientations, these shifts are plotted along with the corresponding χ values in Fig. 7. The shifts K for B_{ext} kagome planes (K_{\parallel}) show behavior similar to that of χ_{\parallel} , increasing monotonically with decreasing temperature. In contrast, K for $B_{\text{ext}} \perp$ kagome planes (K_{\perp}) first increases with decreasing temperature but then deviates from χ_{\perp} below ~ 30 K.

In general, the NMR shift consists of two parts, $K = A_{\text{hf}}\chi_{\text{spin}} + K_{\text{chem}}$, where A_{hf} is the hyperfine coupling constant, χ_{spin} is the local spin susceptibility, and K_{chem} is the temperature independent chemical shift. To calculate A_{hf} , we plot the NMR shift vs bulk χ , with temperature as an implicit parameter (Clogston-Jaccario) [38]. For both the \parallel and the \perp orientations we estimated χ_{\parallel}^i and χ_{\perp}^i using Eqs. (1) and (2) with $\alpha = 0.79$ [see Figs. 7(a) and 7(b)].

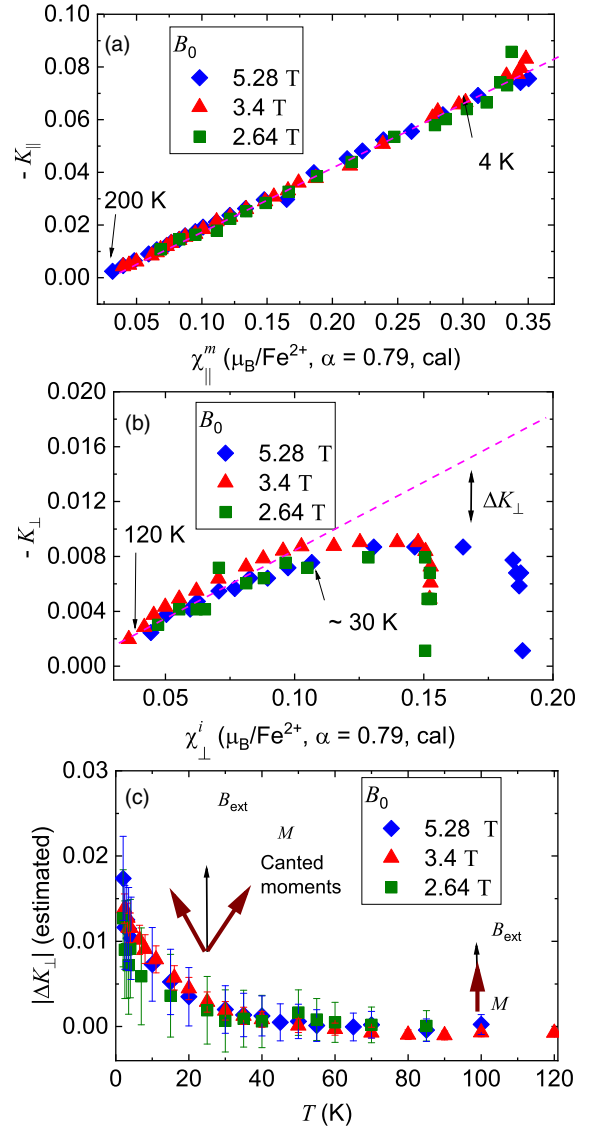


FIG. 8. NMR shift versus macroscopic susceptibility (Clogston-Jaccario plots) for (a) the B_{\parallel} and (b) the B_{\perp} orientations. For B_{\perp} , we performed a comparison by estimating χ_{\perp}^i and χ_{\perp}^i at the respective B_{ext} (2, 3.5, and 5 T) with $\alpha = 0.79$. All dashed lines are guides for the eye. The Clogston-Jaccario plot shows a linear relationship down to 4 K for B_{\parallel} . For \perp , this linear relationship starts to deviate below $T \sim 30$ K. (c) The deviation from linear behavior is plotted as a function of the temperature and shows a tendency to increase as the temperature decreases. We ascribe this increase in the shift to the tilting of the polarized moments toward the kagome planes. These polarized moments are shown as brown arrows in the bottom panel.

The Clogston-Jaccario analysis for \parallel and \perp orientations are shown in Figs. 8(a) and 8(b), respectively. As expected, for the \parallel orientation a strict linear relationship between K and the corresponding bulk susceptibility is observed [Fig. 8(a)]. The NMR shift for the \perp orientation deviates significantly below 30 K [Fig. 8(b)]. The magnitude of this deviation $|\Delta K|$ increases as the temperature is lowered from 30 K [Fig. 8(c)] and decreases with increasing B_{ext} .

In the paramagnetic state and for \perp orientation measurements, the spins are polarized \perp to the kagome planes. The

TABLE I. Calculated A_{dip} tensor elements for one Sn1 and six Sn2 sites as discussed in the text. All values are in units of T/μ_B and are estimated at 120 K for 54 MHz.

	Sn atom						
	Sn1_1	Sn2_1	Sn2_2	Sn2_3	Sn2_4	Sn2_5	Sn2_6
A_{xx}	0.079587(8)	-0.03075(8)	-0.01966(5)	-0.03075(8)	-0.03075(8)	-0.01966(5)	-0.03075(8)
$A_{xy} = A_{yx}$	0.00001(6)	-0.00644(0)	-0.00003(4)	0.00654(6)	-0.00644(0)	-0.00003(4)	0.00654(6)
$A_{xz} = A_{zx}$	0.00000(0)	0.01581(1)	-0.00015(8)	-0.01583(1)	0.01581(1)	-0.00015(8)	-0.01583(1)
A_{yy}	0.079587(8)	-0.02332(1)	-0.03482(3)	-0.02332(1)	-0.02332(1)	-0.03482(3)	-0.02332(1)
$A_{yz} = A_{zy}$	0.00000(0)	-0.00912(7)	0.01819(0)	-0.00895(6)	-0.00912(7)	0.01819(0)	-0.00895(6)
A_{zz}	-0.15915(6)	0.05448(0)	0.05448(9)	0.05448(9)	0.05448(0)	0.05448(9)	0.05448(9)

increase in $|\Delta K|$ below 30 K indicates the onset of tilting of the polarized spins away from the B_{ext} and toward the kagome planes (see Fig. 8). This also confirms the presence of planar anisotropy. This kind of shift can be present due to anisotropic Dzyaloshinskii-Moriya interactions [39]. We discuss the nature of possible in-plane magnetic correlations in Sec. IV.

From the linear fit we calculated the hyperfine coupling constant for both orientations. At $B_0 = 3.4$ T, for the \parallel (\perp) orientation, the calculated $A_{\text{hf},\parallel}$ ($A_{\text{hf},\perp}$) and $K_{\text{chem},\parallel}$ ($K_{\text{chem},\perp}$) are -0.246 ± 0.0028 (-0.171 ± 0.0129) T/μ_B and 0.0065 ± 0.0004 (0.0042 ± 0.0005) T/μ_B . On this basis we conclude that A_{hf} is strongly anisotropic.

For a three-dimensional element with an unquenched orbital moment, both spin and orbital degrees of freedom will contribute to $A_{\text{hf},(\parallel,\perp)}$ and we expect [40]

$$A_{\text{hf},(\parallel,\perp)} = A_{\text{dip},(\parallel,\perp)} + A_{\text{orb},(\parallel,\perp)} + A_{\text{fc},(\parallel,\perp)}. \quad (6)$$

Here A_{dip} , A_{orb} , and A_{fc} represent the contributions from dipolar, orbital, and Fermi contact interactions between Fe and Sn, respectively. Since the Fermi contact term is isotropic in nature we can assume that the anisotropic nature of $\text{Fe}_4\text{Si}_2\text{Sn}_7\text{O}_{16}$ is due to dipolar and orbital interactions.

In the paramagnetic state, we can assume uniform magnetic moments for Fe as $M = [M_x, M_y, M_z]$. We calculated A_{dip} matrix elements $A_{i,j}$ ($i, j = x, y, z$) for all seven Sn sites as shown in Fig. 1(b) (Table I). We performed summation of dipolar contributions over all Fe moments in a sphere centered on the corresponding Sn. The radius of the sphere is large enough (30 times the lattice constant \mathbf{a}) such that all the matrix elements are saturated. Since the major signal contribution is from Sn2 sites, we focus our analysis on the Sn2 dipolar matrix elements.

The calculated diagonal elements A_{xx} and A_{yy} for all Sn2 sites have similar values, in contrast to the corresponding A_{zz} values. The difference in the values of A_{xx} and A_{yy} and significant values of off-diagonal elements will lead to a broadening of the spectrum in the \parallel orientation. For 54 MHz at 120 K this broadening is calculated to be $\sim 0.002(2)$ T, which is smaller compared to the observed width (see Fig. 6). We attribute the additional broadening to a small angular distribution of the oriented polycrystalline sample. Since for all Sn2, $A_{zz} = 0.05448(0)$, we expect a sharp line in the \perp orientation.

In the unoriented sample spectra, the broadening is due to the anisotropic interactions in the system. For 54 MHz we can estimate the line width due to anisotropic dipolar inter-

actions $\Delta_{\text{dip, cal}} = 2\pi \frac{54}{\gamma} |A_{zz}\chi_{(\perp, 120\text{ K})} - (\frac{A_{xx}+A_{yy}}{2})\chi_{(\parallel, 120\text{ K})}| \sim 0.00998$ T, which deviates from the experimentally observed line width, $\Delta_{\text{exp}} \sim 0.014$ T at 120 K, by $\sim 28\%$ (Fig. 6). Since A_{fc} is isotropic in nature we expect that the additional broadening is due to the anisotropy of A_{orb} and K_{chem} . Since $\Delta_{\text{chem, cal}}$ at 120 K is $\sim 0.0014(2)$, we expect $\Delta_{\text{orb}} \sim 0.0026(2)$ T. This shows the presence of significant spin-orbit coupling in $\text{Fe}_4\text{Si}_2\text{Sn}_7\text{O}_{16}$.

D. Spin-lattice relaxation

In Fig. 9 we show the ^{119}Sn spin-lattice relaxation rate as a function of the temperature for oriented samples. These are measured at the maxima of the central lines (Fig. 6). The ^{119}Sn spin-lattice recovery data are well described by the equation

$$m(t) = m(\infty)(1 - Ae^{-t/T_1}), \quad (7)$$

where $m(t)$ is the nuclear magnetization at time t after the first 90° pulse, $m(\infty)$ is the equilibrium nuclear magnetization, and $1/T_1$ is the spin-lattice relaxation rate. For the saturation recovery pulse sequence, ideally $A = 1$ and a full saturation of all the spins is achieved (for details see the Supplemental Material [35]).

In the \parallel orientation, the relaxation rate $(1/T_1)_{B_{\text{ext}}\parallel\text{kagome}}$ remains constant for higher temperatures and starts to decrease significantly below $T \sim 30$ K for all $f = 84, 54,$ and 42 MHz. In contrast to $(1/T_1)_{B_{\text{ext}}\parallel\text{kagome}}$, $(1/T_1)_{B_{\text{ext}}\perp\text{kagome}}$ remains constant above $T \sim 3$ K. In both orientations, we observe a weak maximum at $T \sim 2.5$ K close to the AFM transition due to a critical slowing-down of AFM fluctuations.

In general, $1/T_1$ measures the fluctuating hyperfine fields perpendicular to the applied field described as [41,42]

$$\frac{1}{T_1} \propto \lim_{\omega \rightarrow 0} T \sum_q A_{\text{hf},\perp}^2(q) \frac{\text{Im}\chi^\perp(q, \omega_{\text{NMR}})}{\omega_{\text{NMR}}}, \quad (8)$$

where A_{hf} is the relevant hyperfine form factor and $\text{Im}\chi^\perp(q, \omega_{\text{NMR}})$ represents the \mathbf{q} -dependent imaginary part of the dynamic susceptibility and $\omega_{\text{NMR}} = 2\pi f$. We observe that the peak at $T \sim 2.5$ K is more pronounced for $(1/T_1)_{B_{\text{ext}}\perp\text{kagome}}$ and thus also suggest the dominant formation of correlated spin fluctuations in the kagome planes. Although at a higher field (84 MHz), the AFM peak is suppressed, the anisotropic nature above AFM ordering remains qualitatively similar. This suggests that the anisotropic nature is much more robust to the magnetic field than the observed maxima in χ

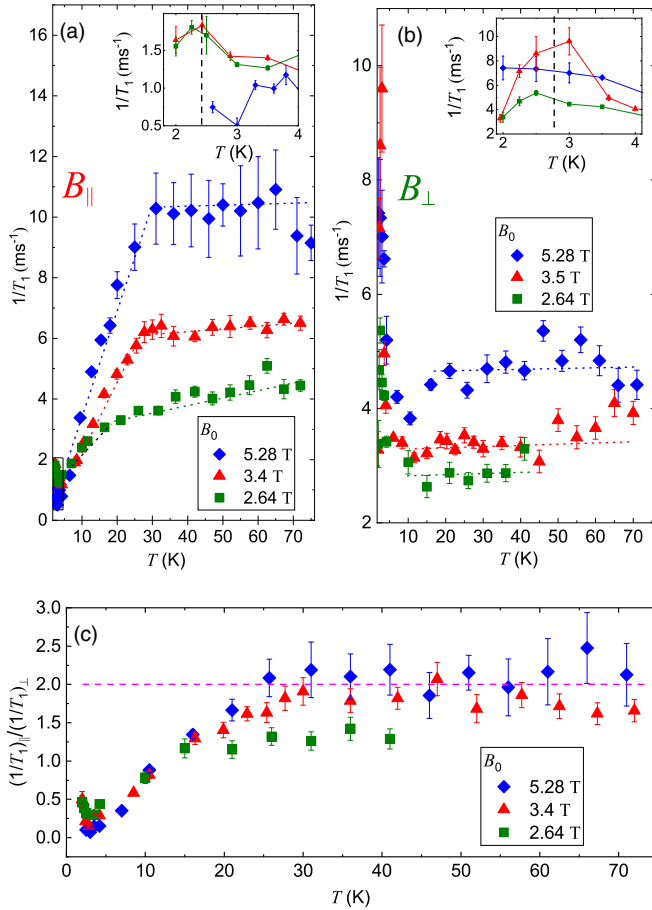


FIG. 9. Temperature dependence of $1/T_1$ measured at $B_0 = 2.64$ T (42 MHz), 3.4 T (54 MHz), and 5.28 T (84 MHz) in (a) the \parallel and (b) the \perp orientation, respectively. For the \parallel orientation, $1/T_1$ starts to decrease at ~ 30 K. Insets: In both orientations for $B_0 = 2.64$ and 3.4 T a small peak is observed around 2–3 K, related to the slowing-down of spin fluctuations near the AFM transition. This peak is enhanced in the \perp orientation. (c) Temperature dependence of the ratio $(1/T_1)_\parallel / (1/T_1)_\perp$. All dashed lines are guides for the eye.

at $T \sim 2.5$ K. In the paramagnetic state ($T > 30$ K) we can assume that $\text{Im}\chi^\pm(q, \omega_{\text{NMR}})$ is isotropic and expect $1/T_1 \propto A_{\text{hf},\perp}^2(q)$. From the calculated dipolar A_{dip} components, the estimated ratio $(1/T_1)_\parallel / (1/T_1)_\perp \sim 2.5$ matches the experimental observations quite well (Fig. 9).

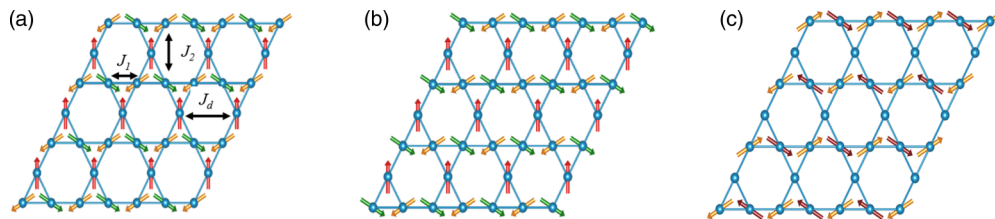


FIG. 10. $\mathbf{q} = (0, 0, 0)$ magnetic ordering with (a) positive and (b) negative chirality. J_1 , J_2 , and J_d show interactions between NN and corresponding further NN interactions, respectively. (c) $\mathbf{q} = (0, 1/2, 0)$ magnetic structure, which is similar to the magnetic structure for $\text{Fe}_4\text{Si}_2\text{Sn}_7\text{O}_{16}$ proposed by Ling *et al.* [15], with $2/3$ ordered moments and $1/3$ disordered moments without AFM ordering along the z axis. Magnetic atoms are shown as blue spheres and arrows represent the magnetic spin on the corresponding atom. Magnetic atoms with disordered moments are represented without a spin vector.

For a fixed temperature, from Eq. (8), we can write $1/T_1 \propto \sum_q A_{\text{hf},\perp}^2(q) \frac{\text{Im}\chi^\pm(q, \omega_{\text{NMR}})}{\omega_{\text{NMR}}}$. At a high temperature, $T \sim 75$ K, we observe that for both orientations, $1/T_1$ increases with the applied field. For the \parallel orientation, we estimated, $A_{\text{hf}}(q = 0, \omega_{\text{NMR}} = \omega_{\text{NMR}}) \sim -0.233 \pm 0.002$, -0.246 ± 0.002 , and -0.245 ± 0.008 T/ μ_B for $B_0 = 5.28$, 3.4, and 2.64 T, respectively. Assuming $A_{\text{hf}}(q, \omega_{\text{NMR}}) \propto A_{\text{hf}}(q = 0, \omega_{\text{NMR}})$, the increase in $1/T_1$ with increasing B_0 suggests that $\text{Im}\chi$ increases more than linearly with respect to ω_{NMR} . This observation is in contrast to the K-jarosite AFM kagome system, in which $1/T_1$ shows frequency-independent behavior in the paramagnetic state. A possible reason for this behavior of $\text{Fe}_4\text{Si}_2\text{Sn}_7\text{O}_{16}$ could be its low value of $\Theta \propto J \sim -12$ K, compared to $\Theta \sim -800$ K in K-jarosite [21,35]. The low J value of $\text{Fe}_4\text{Si}_2\text{Sn}_7\text{O}_{16}$ implies that a B_0 of the order of $\sim T$ is sufficient to change its dynamical properties such that $\text{Im}\chi$ increases with increasing B_0 .

Below 30 K $(1/T_1)_\parallel$ starts to decrease while $(1/T_1)_\perp$ remains constant. This suggests that the hyperfine fluctuations in the z direction start to decrease. From both K and $1/T_1$ measurements we can conclude that magnetic correlations in the kagome plane start to build up below $T \sim 30$ K.

IV. DISCUSSION

In $\text{Fe}_4\text{Si}_2\text{Sn}_7\text{O}_{16}$ below the AFM ordering temperature $T_N \sim 3$ K, only $2/3$ of the total Fe^{2+} moments order, while the other $1/3$ of the Fe^{2+} moments remain disordered down to at least 0.1 K [15]. Further, the observed propagation vector is $\mathbf{q} = (0, 1/2, 1/2)$, which breaks the hexagonal symmetry of the crystal [15]. In the work by Ling *et al.* [15], the experiments were performed on an unoriented sample and the presence of planar anisotropy was extracted from a Rietveld refinement of the neutron powder diffraction pattern. In the present work, we proved the presence of planar anisotropy in NMR experiments on oriented and unoriented samples. Additionally, both K and $1/T_1$ results show the onset of correlations below 30 K.

For the \perp orientation, the NMR shift does not follow a linear relation with χ below 30 K [see Fig. 8(b)]. One possible explanation for this behavior is that the polarized spin moments along the z axis start to tilt into the kagome planes, inducing spin moment components in the kagome planes. To understand the nature of this tilting and the underlying magnetic correlations in the temperature range $3 \text{ K} \lesssim T \lesssim 30 \text{ K}$,

TABLE II. Calculated dipolar field components along the x , y , and z axes. The field is due to Fe^{2+} dipole moments at the Sn sites in T/μ_B and for the three considered magnetic correlations discussed in the text.

Sn	Magnetic correlation								
	I [Fig. 10(a)]			II [Fig. 10(b)]			III [Fig. 10(c)]		
	x	y	z	x	y	z	x	y	z
Sn1_1	−0.000(0)	−0.172(6)	0.000(0)	0.000(0)	−0.000(0)	−0.000(0)	0.000(0)	−0.000(0)	0.000(0)
Sn2_1	0.007(1)	−0.012(2)	0.017(7)	−0.020(2)	−0.011(7)	0.018(1)	0.004(7)	0.007(9)	−0.006(7)
Sn2_2	0.000(1)	0.007(2)	0.018(2)	0.000(3)	−0.023(4)	−0.036(3)	0.005(8)	0.003(4)	0.002(5)
Sn2_3	−0.007(1)	−0.011(9)	0.018(2)	0.020(1)	−0.012(2)	0.018(0)	−0.002(8)	−0.003(5)	0.0131(9)
Sn2_4	0.007(1)	−0.012(1)	0.017(7)	−0.020(2)	−0.011(6)	0.018(1)	0.004(7)	0.007(9)	−0.006(7)
Sn2_5	−0.007(1)	−0.011(9)	0.018(1)	−0.020(1)	−0.012(0)	−0.018(0)	−0.002(8)	−0.003(5)	0.0131(0)
Sn2_6	0.000(2)	0.000(8)	0.018(2)	0.000(4)	0.023(5)	−0.036(3)	0.005(8)	0.003(3)	0.002(6)

we performed dipolar field calculations for three magnetic correlations in the kagome plane. Within our experimental temperature range, no line splitting is observed in the NMR spectrum. Therefore, we considered three magnetic correlations which would not lead to any such splitting. The first two of these correspond to 120° -type $\mathbf{q} = \mathbf{0}$ magnetic structures with positive and negative vector chiralities [Figs. 10(a) and 10(b)] [21]. The third considered magnetic correlation is shown in Fig. 10(c) and is similar to the magnetic structure as predicted by Ling *et al.* [15] without AFM correlations along the z axis [i.e., $\mathbf{q} = (0, 1/2, 0)$].

The results of dipole field calculations for three considered magnetic correlations are listed in Table II. Recall that in the \perp orientation, for all Sn2 the calculated $A_{zz} = -0.05448(0) T/\mu_B$ (see Table I). Further, below 30 K, K for the \perp orientation starts to become less negative. From this we expect that the magnetic correlations will induce a positive z component of the internal field. Additionally, a clear indication of peak splitting is not observed. Only for case I is a consistent and homogeneous positive value of the z component found for all Sn2 sites. For cases II and III, the calculated negative values of the z components (II) for some Sn2 sites will result in a splitting and/or broadening of the peak which is not observed in the NMR spectrum. Therefore, among the considered magnetic correlations, our calculations suggest that positive chiral magnetic correlations start to build up below 30 K [see Fig. 10(a)].

From our bulk magnetization and NMR measurements on oriented powder, we cannot distinguish between global easy-plane anisotropy and the presence of multiple local Ising axes in the kagome planes (as in the kagome spin-ice model, where the local Ising axis points towards the line joining the center of two triangles [18]). In kagome spin ice, frustration arises due to Ising anisotropy combined with NN ferromagnetic interactions [43,44]. For this model with additional NNN interactions (J_2), Wills *et al.* [18] predicted partially ordered magnetic states for both ferromagnetic ($J_2 > 0$) and AFM ($J_2 < 0$) cases. While for $\text{Fe}_4\text{Si}_2\text{Sn}_7\text{O}_{16}$ all the calculated Θ_{CW} values are AFM, the possibility of a kagome spin-ice model cannot be ignored because the Fe1 sites in the kagome planes are not perfectly octahedrally coordinated by the surrounding O1 and O3 sites [35]. Additionally, since a Sn ion is present at the center of each kagome ring, the diagonal exchange term J_d

[see Fig. 10(a)] can also be relevant to the observed partially ordered ground state of $\text{Fe}_4\text{Si}_2\text{Sn}_7\text{O}_{16}$.

V. CONCLUSIONS

In this work, we present ZFC magnetic susceptibility and NMR measurements on unoriented and oriented powder samples of $\text{Fe}_4\text{Si}_2\text{Sn}_7\text{O}_{16}$. For both orientations, anisotropic behavior prevails at least up to $B_{\text{ext}} = 5$ T. The detailed Curie-Weiss law analysis in the \parallel (\perp) orientation shows $\mu_{\text{eff, Fe}^{2+}} \sim 5.25\mu_B$ ($5.15\mu_B$) $> \mu_{\text{spin}} = 4.9\mu_B$, therefore significant spin-orbit coupling is present. All the estimated Θ_{CW} 's are negative, indicating that AFM interactions are dominant.

In NMR measurements, we show the presence of planar magnetic anisotropy in $\text{Fe}_4\text{Si}_2\text{Sn}_7\text{O}_{16}$. Both K and $1/T_1$ are highly anisotropic. While in the \parallel orientation the Clogston-Jaccario plots exhibits a linear relationship between K and χ down to 4 K, in the \perp orientation it starts to deviate below 30 K. This deviation increases as the temperature is lowered. We associate this with a tilting of polarized z moments towards the kagome plane. Our dipolar analysis suggests that magnetic correlations with positive vector chirality start to develop below 30 K. These correlations are also observed in $1/T_1$ measurements, as $(1/T_1)_{\parallel}$ starts to decrease below 30 K. At lower temperatures, peaks associated with the slowing-down of spin fluctuations are observed for both orientations. This peak is more pronounced in the \perp orientation and thus further demonstrates the dominance of AFM interactions in the kagome planes.

ACKNOWLEDGMENTS

We acknowledge helpful discussions with F. Brückner and S. Dey. This work was supported by the Deutsche Forschungsgemeinschaft (DFG) through Grant Nos. SFB 1143 and GRK 1621, the Australian Research Council (ARC) through Grant No. DP190101862, the Alexander von Humboldt Foundation through a Friedrich Wilhelm Bessel Research Award to C. D. Ling, and the Dresden High Magnetic Field Laboratory (HLD) at HZDR, member of the European Magnetic Field Laboratory (EMFL).

- [1] P. Mendels and F. Bert, *Compt. Rend. Phys.* **17**, 455 (2016).
- [2] K. Essafi, O. Benton, and L. D. C. Jaubert, *Nat. Commun.* **7**, 10297 (2016).
- [3] J. T. Chalker, P. C. W. Holdsworth, and E. F. Shender, *Phys. Rev. Lett.* **68**, 855 (1992).
- [4] A. B. Harris, C. Kallin, and A. J. Berlinsky, *Phys. Rev. B* **45**, 2899 (1992).
- [5] J. Rehn, A. Sen, and R. Moessner, *Phys. Rev. Lett.* **118**, 047201 (2017).
- [6] T. Bilitewski, M. E. Zhitomirsky, and R. Moessner, *Phys. Rev. Lett.* **119**, 247201 (2017).
- [7] R. R. P. Singh and D. A. Huse, *Phys. Rev. B* **77**, 144415 (2008).
- [8] Y. Ran, M. Hermele, P. A. Lee, and X.-G. Wen, *Phys. Rev. Lett.* **98**, 117205 (2007).
- [9] L. Messio, B. Bernu, and C. Lhuillier, *Phys. Rev. Lett.* **108**, 207204 (2012).
- [10] S. T. Bramwell, *Science* **294**, 1495 (2001).
- [11] J. S. Gardner, M. J. P. Gingras, and J. E. Greedan, *Rev. Mod. Phys.* **82**, 53 (2010).
- [12] T. Söhnel, P. Böttcher, W. Reichelt, and F. E. Wagner, *Z. anorg. allg. Chem.* **624**, 708 (1998).
- [13] M. C. Allison, M. Avdeev, S. Schmid, S. Liu, T. Söhnel, and C. D. Ling, *Dalton Trans.* **45**, 9689 (2016).
- [14] M. P. Shores, E. A. Nytko, B. M. Bartlett, and D. G. Nocera, *J. Am. Chem. Soc.* **127**, 13462 (2005).
- [15] C. D. Ling, M. C. Allison, S. Schmid, M. Avdeev, J. S. Gardner, C.-W. Wang, D. H. Ryan, M. Zbiri, and T. Söhnel, *Phys. Rev. B* **96**, 180410(R) (2017).
- [16] J. D. M. Champion, A. S. Wills, T. Fennell, S. T. Bramwell, J. S. Gardner, and M. A. Green, *Phys. Rev. B* **64**, 140407(R) (2001).
- [17] A. Oyamada, S. Maegawa, M. Nishiyama, H. Kitazawa, and Y. Isikawa, *Phys. Rev. B* **77**, 064432 (2008).
- [18] A. S. Wills, R. Ballou, and C. Lacroix, *Phys. Rev. B* **66**, 144407 (2002).
- [19] L. Messio, C. Lhuillier, and G. Misguich, *Phys. Rev. B* **83**, 184401 (2011).
- [20] T. Inami, M. Nishiyama, S. Maegawa, and Y. Oka, *Phys. Rev. B* **61**, 12181 (2000).
- [21] M. Nishiyama, S. Maegawa, T. Inami, and Y. Oka, *Phys. Rev. B* **67**, 224435 (2003).
- [22] D. Grohol, K. Matan, J.-H. Cho, S.-H. Lee, J. W. Lynn, D. G. Nocera, and Y. S. Lee, *Nat. Mater.* **4**, 323 (2005).
- [23] S. Sachdev, *Phys. Rev. B* **45**, 12377 (1992).
- [24] M. Elhadj, B. Canals, and C. Lacroix, *Phys. Rev. B* **66**, 014422 (2002).
- [25] K. Matan, D. Grohol, D. G. Nocera, T. Yildirim, A. B. Harris, S. H. Lee, S. E. Nagler, and Y. S. Lee, *Phys. Rev. Lett.* **96**, 247201 (2006).
- [26] T. Yildirim and A. B. Harris, *Phys. Rev. B* **73**, 214446 (2006).
- [27] K. Matan, B. M. Bartlett, J. S. Helton, V. Sikolenko, S. Mat'as, K. Prokeš, Y. Chen, J. W. Lynn, D. Grohol, T. J. Sato, M. Tokunaga, D. G. Nocera, and Y. S. Lee, *Phys. Rev. B* **83**, 214406 (2011).
- [28] M. A. de Vries, T. K. Johal, A. Mirone, J. S. Claydon, G. J. Nilsson, H. M. Rønnow, G. van der Laan, and A. Harrison, *Phys. Rev. B* **79**, 045102 (2009).
- [29] M. O. Ajeesh, T. Shang, W. B. Jiang, W. Xie, R. D. dos Reis, M. Smidman, C. Geibel, H. Q. Yuan, and M. Nicklas, *Sci. Rep.* **7**, 7338 (2017).
- [30] Z. L. Dun, X. Li, R. S. Freitas, E. Arrighi, C. R. Dela Cruz, M. Lee, E. S. Choi, H. B. Cao, H. J. Silverstein, C. R. Wiebe, J. G. Cheng, and H. D. Zhou, *Phys. Rev. B* **92**, 140407(R) (2015).
- [31] A. M. Hallas, J. Gaudet, and B. D. Gaulin, *Ann. Rev. Condens. Matter Phys.* **9**, 105 (2018).
- [32] O. Ofer and A. Keren, *Phys. Rev. B* **79**, 134424 (2009).
- [33] E.-W. Scheidt, C. Hucho, K. Lüders, and V. Müller, *Solid State Commun.* **71**, 505 (1989).
- [34] S. Horii, A. Ishihara, T. Fukushima, T. Uchikoshi, H. Ogino, T. S. Suzuki, Y. Sakka, J.-I. Shimoyama, and K. Kishio, *Sci. Technol. Adv. Mater.* **10**, 014604 (2009).
- [35] See Supplemental Material at <http://link.aps.org/supplemental/10.1103/PhysRevB.103.064425> for bulk magnetization data up to $B_{\text{ext}} = 5$ T along with the Curie-Weiss law analysis and the local crystal environment of kagome Fe.
- [36] D. Boldrin, B. Fåk, E. Canévet, J. Ollivier, H. Walker, P. Manuel, D. Khalyavin, and A. Wills, *Phys. Rev. Lett.* **121**, 107203 (2018).
- [37] H. Ishikawa, T. Yajima, A. Miyake, M. Tokunaga, A. Matsuo, K. Kindo, and Z. Hiroi, *Chem. Mater.* **29**, 6719 (2017).
- [38] A. M. Clogston, V. Jaccarino, and Y. Yafet, *Phys. Rev.* **134**, A650 (1964).
- [39] A. U. B. Wolter, P. Wzietek, S. Süllow, F. J. Litterst, A. Honecker, W. Brenig, R. Feyerherm, and H.-H. Klauss, *Phys. Rev. Lett.* **94**, 057204 (2005).
- [40] D. M. Nisson and N. J. Curro, *New J. Phys.* **18**, 073041 (2016).
- [41] T. Moriya, *Prog. Theor. Phys.* **16**, 23 (1956).
- [42] K. Kitagawa, N. Katayama, K. Ohgushi, M. Yoshida, and M. Takigawa, *J. Phys. Soc. Jpn.* **77**, 114709 (2008).
- [43] J. Carrasquilla, Z. Hao, and R. G. Melko, *Nat. Commun.* **6**, 7421 (2015).
- [44] J. A. M. Paddison, H. S. Ong, J. O. Hamp, P. Mukherjee, X. Bai, M. G. Tucker, N. P. Butch, C. Castelnovo, M. Mourigal, and S. E. Dutton, *Nat. Commun.* **7**, 13842 (2016).